THE ASTROPHYSICAL JOURNAL, 563:1063–1074, 2001 December 20

MUTUAL EVENT OBSERVATIONS OF IO'S SODIUM CORONA

M. H. BURGER AND N. M. SCHNEIDER
Laboratory for Atmospheric and Space Physics, University of Colorado, Boulder, CO 80309;
burger@ganesh.colorado.edu, nick@hanuman.colorado.edu

I. DE PATER
Department of Astronomy, University of California, Berkeley, CA 94720; imke@floris.berkeley.edu

M. E. BROWN AND A. H. BOUCHEZ
Division of Geological and Planetary Sciences, California Institute of Technology, Pasadena, CA 91125;
mbrown@gps.caltech.edu, antonin@gps.caltech.edu

L. M. TRAFTON, Y. SHEFFER, AND E. S. BARKER
Astronomy Department, University of Texas, Austin, TX 78712; lmt@astro.as.utexas.edu, yaron@anchor.as.utexas.edu, ebs@astro.as.utexas.edu

AND

A. MALLAMA
Raytheon Information Technology and Scientific Services, Lanham, MD 20706; anthony_mallama@raytheon.com
Received 2000 October 6; accepted 2001 August 17

ABSTRACT

We have measured the column density profile of Io's sodium corona using 10 mutual eclipses between the Galilean satellites. This approach circumvents the problem of spatially resolving Io's corona directly from Io's bright continuum in the presence of atmospheric seeing and telescopic scattering. The primary goal is to investigate the spatial and temporal variations of Io's corona. Spectra from the Keck Observatory and McDonald Observatory from 1997 reveal a corona that is only approximately spherically symmetric around Io. Comparing the globally averaged radial sodium column density profile in the corona with profiles measured in 1991 and 1985, we find that there has been no significant variation. However, there appears to be a previously undetected asymmetry: the corona above Io's sub-Jupiter hemisphere is consistently more dense than above the anti-Jupiter hemisphere.

Subject headings: planets and satellites: individual (Io) — techniques: spectroscopic

On-line material: machine-readable table

1. INTRODUCTION

Io's volcanic atmosphere is dominated by SO_2 and atomic sulfur and oxygen (reviewed by Spencer & Schneider 1996; Lellouch 1996). Spectra of Io's surface with the *Hubble Space Telescope* (*HST*) have detected SO_2 gas in the atmosphere at three discrete regions representing three distinct areas of Io's surface (volcanic plumes, SO_2 frost, and a region with neither plumes nor frost), implying global SO_2 coverage (McGrath et al. 2000). Additionally, images of Lyα emission from Io using the *HST*/Space Telescope Imaging Spectrograph have been interpreted as showing reflected solar Lyα emission attenuated by an SO_2 atmosphere. These images show a global atmosphere with SO_2 gas concentrated near the equator (Feldman et al. 2000). Results from the *Galileo* spacecraft support this suggestion with observations indicating that Io has a global ionosphere (Hinson et al. 1998) that may be denser near the equatorial regions (Burger, Schneider, & Wilson 1999)

Where Io's gravity dominates over Jupiter's, within about 6 Io radii ($6R_{Io}$), there is a corona (or exosphere) consisting of atoms and molecules that are gravitationally bound to Io. The density is much lower than the near-surface component, and there is little interaction between the constituents. The inner boundary of the corona is defined by Io's exobase, the distance from Io at which collisions between atoms are no longer important. Constituents that leave the exobase with velocities greater than the escape velocity or are accelerated to escape velocity by interactions with plasma torus ions can escape from the corona. A mapping of the sodium corona (Schneider et al. 1991) has shown that this region is roughly spherically symmetric about Io.

Neutral sodium was first discovered at Io more than 25 yr ago (Brown 1974; Trafton, Parkinson, & Macy 1974). Despite its small abundance, optical wavelength observations of sodium have been essential for understanding the structure and escape of Io's atmosphere because of the challenges in measuring the densities of the major atmospheric species. The emission from the dominant coronal species, oxygen and sulfur, results from electron impact excitation, so the observed emission is a function of the neutral density, electron density, and electron temperature, making the neutral density profile difficult to determine directly from observational data without detailed modeling. Because the sodium D lines are formed through a resonant transition, sodium can be observed at Io in both emission and absorption. Also, sodium emission is much brighter than emission by the other atmospheric components. Therefore, optical wavelength observations of sodium have been essential for understanding the structure and escape of Io's atmosphere.

Sodium is now known to escape through "slow" and "fast" processes. Sputtering of neutrals off the atmosphere and corona form an extended cloud of slowly escaping neutrals (mean velocity $\sim$2–3 km s^{-1} with a high-speed tail extending to $\sim$10–30 km s^{-1}), which primarily leads Io in its orbit around Jupiter (Smyth 1992). Similar clouds are known to exist for the more dominant species of sulfur and

oxygen (Brown 1981; Thomas 1996) but have not been well studied since emission from these species is at the limits of what can be observed. There are several mechanisms that result in the fast escape of sodium (velocity $\gtrsim 10$ km s^{-1}). Jupiter's magnetic field accelerates sodium ions in Io's collisionally thick ionosphere that are neutralized through charge exchange to produce fast neutrals (Wilson & Schneider 1999). Sodium ions in the plasma torus can also charge exchange with neutrals to create fast sodium. Similarly, sodium-bearing molecular ions are swept into the torus of plasma that encircles Jupiter, and dissociation of these molecules creates a separate fast-sodium feature (Wilson & Schneider 1994). Additional fast sodium results from the high-speed tail of the sputtering flux distribution (Smyth 1992).

Tracing the distribution of sodium in the corona will help to explain the sources and escape of all coronal species. Although oxygen and sulfur have been detected in the corona (Ballester et al. 1987), the radial density profiles of these species have never been measured owing to the difficulties discussed above. Recent observations with *HST* have mapped the intensity profile within $10R_{\rm Io}$ (Roesler et al. 1999; Wolven et al. 2001). Saur et al. (2000) have shown that the qualitative features of the bright equatorial emission spots seen in observations of neutral oxygen (O I] 1356 Å) (Retherford et al. 2000) close to Io can be explained through interactions between Io and the plasma torus in a spherically symmetric corona. This is an indication of the difficulties involved in deriving a unique oxygen density profile from remote observations. Since the sodium abundance is more directly determined from intensity, observations of the sodium corona provide a less ambiguous view of the near-Io environment.

In this paper the distribution of sodium in Io's corona is measured using spectra taken of Galilean satellites being eclipsed by Io. Data from 1991 and 1997 are compared with the previous mapping in 1985 by Schneider et al. (1991) to show that the corona has remained remarkably stable over a period of 12 yr. We also present evidence for an apparent column density asymmetry in the corona above Io's sub-Jupiter and anti-Jupiter hemispheres.

2. OBSERVATIONS

Under normal viewing conditions it is not possible to observe sodium close to Io's surface. This is primarily due to two effects: First, Io has a very high geometric albedo. The surface is approximately as bright in backscattered sunlight at 5900 Å as an optically thick sodium atmosphere. Therefore, Io's disk looks the same regardless of how much sodium is present (Brown, Murcray, & Chaffee 1975). Second, the Earth's atmosphere smears the emission on scales of the order of a few Io radii ($R_{\rm Io}$) in such a way as to significantly alter the observed emission profile (Schneider et al. 1991).

To circumvent these problems, we have taken advantage of mutual eclipsing events between the Galilean satellites following the method of Schneider et al. (1987, 1991). The plane of Jupiter's satellites crosses the Sun-Jupiter plane twice along Jupiter's 12 yr orbit around the Sun. This provides an opportunity to apply a unique method of probing the exospheres of the moons. As the eclipsing moon (e.g., Io as shown in Fig. 1) passes between the Sun and the eclipsed moon (Europa in Fig. 1), the light that is not physically blocked by Io's surface passes through its corona. Sodium atoms in this region scatter the solar photons. This light then reflects off Europa and is observed at Earth. Spectra taken of Europa show the sodium absorption feature from Io's corona. A comparison of spectra taken during and outside of eclipse provides a time series of how much absorption took place during different light traversal paths through Io's corona (Fig. 2).

We use a series of observations of Galilean satellites being eclipsed by Io from the 1997 eclipse season taken at the Keck Observatory in Hawaii and McDonald Observatory in Texas, as well as one event observed from the Catalina Observatory in Arizona in 1991. The data sets are discussed in detail below. Table 1 lists the events observed for this analysis. Io's orbital geometry for each observation is shown in Figure 3. Although most of the events are clustered near Io's western elongation (orbital phase $\sim 270°$), a variety of orbital geometries are represented. Each event measures a different cut through Io's corona, and each

TABLE 1

ECLIPSE PARAMETERS

Eclipse Number	Date	UT[a]	Duration[b] (minutes)	Telescope	Eclipsed Satellite	Minimum b[c] ($R_{\rm Io}$)	$\phi_{\rm Io}$(helio)[d] (deg)	$\phi_{\rm Io}$(geo)[e] (deg)	$\lambda_{\rm III,\ Io}$[f] (deg)
1	1997 Jun 21	15:32	17.1	Keck	Callisto	2.1	347	337	314
2	1997 Aug 27	8:10	4.5	Keck	Callisto	3.1	233	235	162
3	1997 Aug 27	11:30	13.8	Keck	Ganymede	1.4	261	263	256
4	1997 Jun 19	7:57	6.0	McDonald	Europa	1.2	236	226	209
5	1997 Jul 21	6:24	2.5	McDonald	Europa	2.1	252	247	273
6	1997 Aug 20	8:09	10.6	McDonald	Ganymede	1.6	249	251	173
7	1997 Aug 30	2:35	8.6	McDonald	Europa	1.9	76	80	208
8	1997 Oct 3	1:25	7.6	McDonald	Ganymede	1.6	141	150	175
9	1997 Oct 10	4:15	6.6	McDonald	Ganymede	2.0	149	159	242
10	1991 May 21	3:59[g]	5.5[g]	Catalina	Europa	1.2	227	235	341

[a] Universal Time of eclipse midpoint; from Arlot 1996 except as noted.
[b] Duration of event; from Arlot 1996 except as noted.
[c] Minimum impact parameter of the event (see text for details).
[d] Io's heliocentric orbital longitude at eclipse midpoint.
[e] Io's geocentric orbital longitude at eclipse midpoint.
[f] Io's magnetic (system III) longitude at eclipse midpoint.
[g] From J.-E. Arlot 1999, private communication.

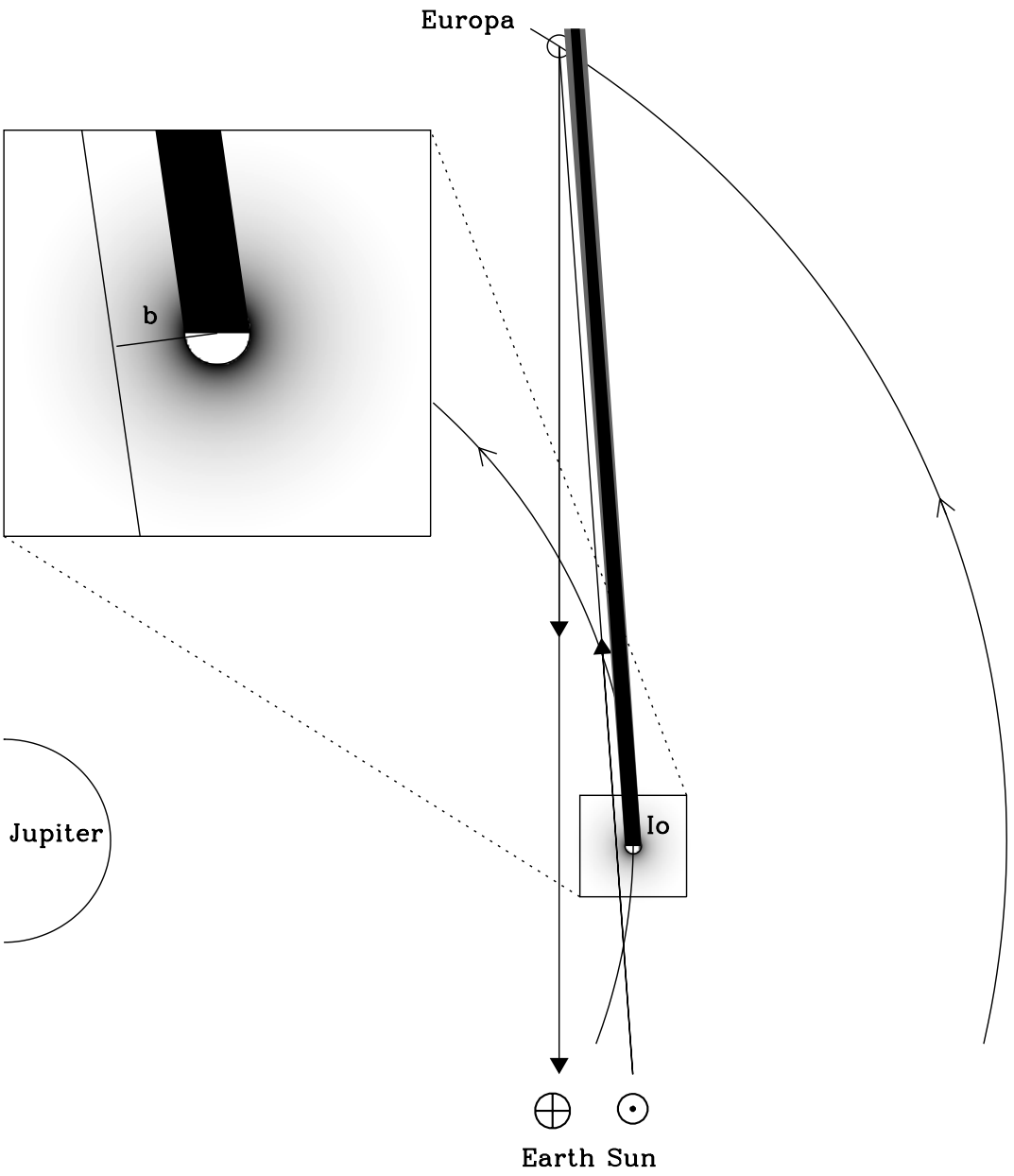

FIG. 1.—Sketch of Io eclipsing Europa. Sunlight passes through the corona, reflects off Europa, and is observed at the Earth. Io's umbra and penumbra are shown falling on Europa. The shaded region surrounding Io represents Io's sodium corona. The extended sodium neutral cloud that leads Io in its orbit is not shown. Io, Europa, and the corona are drawn at 3 times the scale of Jupiter and the satellite orbits. The direction of satellite motion is indicated, although the magnitude of motion during an observation is not. The insert shows the size of the impact parameter for the observation.

observation samples a different section along this trajectory, giving us a chance to probe the three-dimensional geometry of the corona. Table 2 lists the location relative to Io of each observation. The determination of the radial distance from Io sampled (the impact parameter b) is discussed in § 3 below.

2.1. *Keck Observatory Observations*

Three mutual events were observed from the 10 m telescope at the Keck Observatory using the High-Resolution Echelle Spectrometer (HIRES); (Vogt 1994), an echelle spectrograph with a cross disperser. At the sodium D line wavelengths ($\sim$5900 Å), the spectral resolution is $\lambda/\Delta\lambda \sim 67{,}000$ corresponding to a full width at half-maximum (FWHM) for a monochromatic source of 2.0 pixels, or 88 mÅ. The signal-to-noise ratio for a 70 s exposure is $\sim$450 for the continuum near the sodium D lines and $\sim$115 at the minima of the deep Fraunhofer absorption lines.

The reduction of the spectra proceeded as follows to determine the equivalent widths of the coronal sodium absorption lines: the spectra were first bias subtracted and flat-field corrected in the standard way. Because the light from the observed moon did not cover the entire length of the slit, we were able to subtract background light from the spectra. For each column along the spectral direction, the slice along the spatial direction was approximated by a Gaussian plus a polynomial, with the Gaussian approximating the light from the satellite and the polynomial that from the background. We used this primitive fit simply to identify the region of sky along the column and then per-

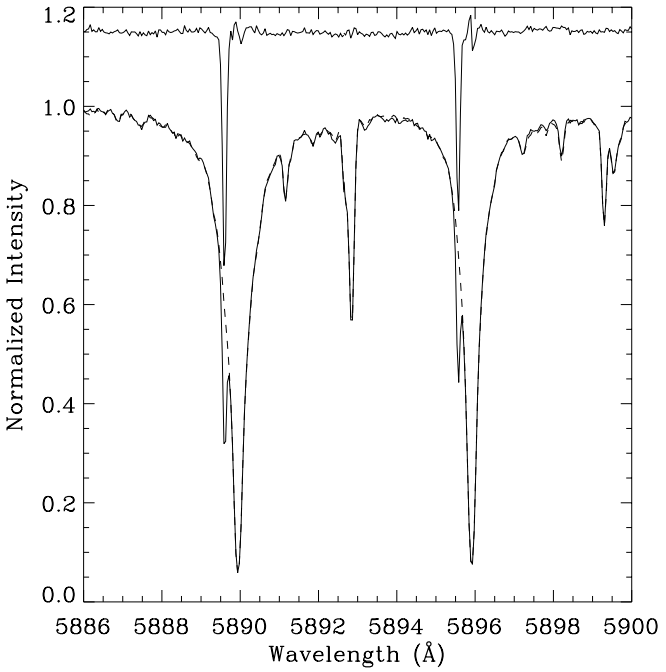

FIG. 2.—Removal of the solar spectrum from an observation from Keck Observatory on 1997 August 27. *Lower solid line*: Spectrum of Callisto (spectrum 3.10 from Table 2) during an eclipse showing the absorption from Io's corona. *Dashed line*: Spectrum of Callisto out of eclipse (with no absorption at Io). *Upper solid line*: Ratio of the two spectra showing a pure Io spectrum. The core of the solar Fraunhofer line is not removed perfectly, but the Doppler shift between the Io sodium absorption line and the solar line is sufficient that the Iogenic absorption is not affected. This line has been shifted up by 0.15 for clarity. Separate corrections are made for the D_2 and D_1 lines. Wavelength calibration is based on the solar rest frame.

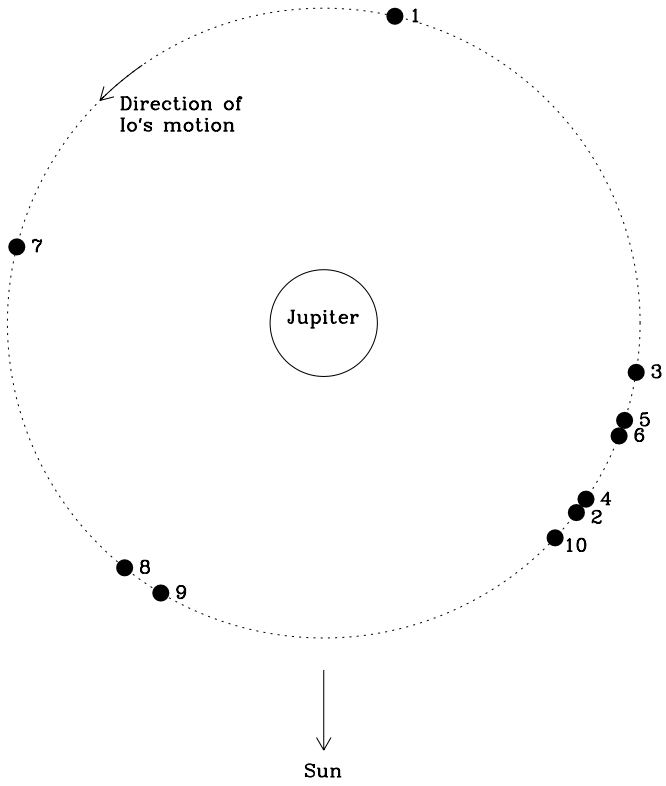

FIG. 3.—Io's orbital geometry for each of the observed mutual events listed in Table 1 as observed from the Sun. Io is not shown to scale. Event numbers are indicated. Direction to Earth varies for different observing dates.

formed a χ^2 minimization routine to fit a low-order polynomial to the sky. By fitting a separate polynomial for each column along the spectral dimension, we subtracted the wavelength-dependent background, including the spatially uniform emission from sodium in the Earth's atmosphere. After subtracting the background, the spectra were reduced to one dimension by summing in the spatial direction. This process was performed on all the spectra during the eclipse series plus several spectra taken out of eclipse that were used as solar references to isolate the absorption at Io.

After producing a spectrum, light scattered in the optics of the spectrograph, which fills in the bottom of the Fraunhofer lines, was removed (Vogt 1994). Neglecting this effect underestimates the amount of absorption and therefore the column density of sodium. An empirical correction was performed by matching the spectra to a standard high-resolution solar spectrum convolved with the HIRES point-spread function. The bases of the solar Fraunhofer absorption lines were 5% of the continuum (Brown & Yung 1976).

The solar spectrum was removed by matching the spectra taken during eclipses with a reference spectrum of the same object taken out of eclipse. The reference was shifted by subpixel amounts to account for small wavelength shifts between observations. Dividing an eclipse spectrum by the pure solar spectrum revealed the absorption from sodium in the corona (Fig. 2). Separate corrections were made to remove the solar spectrum around the D_2 and D_1 lines. Telluric absorptions are negligible in the Keck data near the Iogenic sodium absorption lines, so no further corrections were needed.

A wavelength calibration was made by identification of solar absorption lines (Moore, Minnaert, & Houtgast 1966). The resulting calibration gave the wavelengths in the solar rest frame rather than in the observer's rest frame but allowed for the determination of slight shifts in wavelength between observations. The wavelength calibration is accurate to within 0.05 Å.

2.2. *McDonald Observatory Observations*

Six mutual events were recorded with the 2.7 m telescope at the McDonald Observatory using the two-dimensional Coudé Echelle Spectrometer. The events were split evenly between Europa and Ganymede as the eclipsed satellite. Typical spectral resolution attained was $\lambda/\Delta\lambda \sim 60{,}000$ (as determined from the FWHM of telluric lines in the program spectra). Exposures were 60 s in length, yielding signal-to-noise ratio levels of ~ 100 in the continuum.

Standard reduction and analysis procedures were followed in the Image Reduction and Analysis Facility (IRAF) environment, starting with bias subtraction and flat-field division. The echelle order with the sodium D lines was traced and extracted in order to create a one-dimensional spectrum. Owing to order-spacing constraints, it was not possible to distinguish between sky background and scattered light, and the regions toward the ends of the slit were avoided in the one-dimensional summation. Scattered light in the spectrograph was removed using the method described above for the Keck observations.

McDonald spectra are usually "wet"; i.e., they include an appreciable number of telluric water lines. This contamination was easily removed by a division of all one-dimensional spectra by a spectrum of a hot star observed on the same night. Despite variations in air mass toward differ-

TABLE 2

SUMMARY OF ECLIPSE OBSERVATIONS

Observation Number[a]	Phase[b]	b[c] (R_{Io})	Location[d]	Wavelength of D2 (mÅ)	Wavelength of D1 (mÅ)	N (cm^{-2})	T[e] (K)
1.0.....	0.2	2.5	L, N	14 ± 2	6 ± 2	$(7 \pm 1) \times 10^{10}$	Thin
1.1.....	0.2	2.4	L, N	9 ± 2	17 ± 4	$(6 \pm 2) \times 10^{10}$	Thin
1.2.....	0.3	2.2	L, N	13 ± 4	9 ± 2	$1.3^{+0.5}_{-0.3} \times 10^{11}$	Undetermined
1.3.....	0.3	2.2	L, N	20 ± 4	25 ± 2	$(2 \pm 1) \times 10^{11}$	Undetermined
1.4.....	0.4	2.1	L, N	24 ± 4	26 ± 2	$(2 \pm 1) \times 10^{11}$	Undetermined
1.5.....	0.5	2.1	N	25 ± 4	17 ± 5	$2.6^{+1.5}_{-0.8} \times 10^{11}$	<1200
2.0.....	−1.9	7.7	A, L, N	3.4 ± 0.5	3.3 ± 0.5	$(2.2 \pm 0.3) \times 10^{10}$	Thin
2.1.....	−1.5	6.6	A, L, N	6.2 ± 0.5	3.9 ± 0.4	$(3.4 \pm 0.3) \times 10^{10}$	Thin
2.2.....	−1.1	5.5	A, L, N	10.0 ± 0.6	4.2 ± 0.5	$(5.0 \pm 0.3) \times 10^{10}$	Thin
2.3.....	−0.6	4.6	A, L, N	13.6 ± 0.6	6.8 ± 0.5	$(7.2 \pm 0.3) \times 10^{10}$	Thin
2.4.....	−0.2	3.7	A, L, N	22.2 ± 0.6	10.8 ± 0.5	$(1.18 \pm 0.06) \times 10^{11}$	Undetermined
2.5.....	0.3	3.2	A, L, N	28.4 ± 0.6	16.9 ± 0.4	$(2.04 \pm 0.12) \times 10^{11}$	900^{+700}_{-400}
2.6.....	0.7	3.2	J, T, N	28.6 ± 0.6	16.1 ± 0.4	$(1.86 \pm 0.11) \times 10^{11}$	2000^{+2200}_{-900}
2.7.....	1.2	3.8	J, T, N	20.2 ± 0.6	11.2 ± 0.5	$1.27^{+0.12}_{-0.10} \times 10^{11}$	1100^{+4000}_{-800}
2.8.....	1.6	4.6	J, T, N	12.9 ± 0.6	6.5 ± 0.4	$6.7^{+0.9}_{-0.2} \times 10^{10}$	Undetermined
2.9.....	2.1	5.4	J, T, N	9.1 ± 0.6	5.4 ± 0.4	$(5.1 \pm 0.3) \times 10^{10}$	Thin
2.10	2.5	6.5	J, T, N	6.2 ± 0.6	2.4 ± 0.5	$(3.0 \pm 0.3) \times 10^{10}$	Thin
2.11	2.9	7.6	J, T, N	3.3 ± 0.5	1.1 ± 0.4	$(1.6 \pm 0.2) \times 10^{10}$	Thin
2.12	3.3	8.7	J, T, N	3.2 ± 0.6	0.2 ± 0.4	$1.7 \pm 0.3 \times 10^{10}$	Thin
3.0.....	−1.2	>10	A, S	1.0 ± 0.4	1.4 ± 0.4	$(6.7 \pm 2.4) \times 10^{9}$	Thin
3.1.....	−1.1	>10	A, S	1.7 ± 0.4	2.0 ± 0.4	$(1.1 \pm 0.2) \times 10^{10}$	Thin
3.2.....	−0.9	8.1	A, S	2.0 ± 0.4	1.8 ± 0.4	$(1.2 \pm 0.2) \times 10^{10}$	Thin
3.3.....	−0.7	7.2	A, S	1.4 ± 0.4	2.0 ± 0.4	$(1.0 \pm 0.2) \times 10^{10}$	Thin
3.4.....	−0.6	6.4	A, S	4.6 ± 0.5	2.4 ± 0.4	$(2.4 \pm 0.2) \times 10^{10}$	Thin
3.5.....	−0.4	5.5	A, S	6.1 ± 0.6	3.0 ± 0.4	$(3.1 \pm 0.3) \times 10^{10}$	Thin
3.6.....	−0.3	4.7	A, S	8.0 ± 0.5	3.8 ± 0.4	$(4.1 \pm 0.3) \times 10^{10}$	Thin
3.7.....	−0.1	3.8	A, S	11.2 ± 0.5	6.0 ± 0.5	$6.5^{+1.2}_{-0.8} \times 10^{10}$	Undetermined
3.8.....	0.0	3.0	A, S	18.8 ± 0.5	10.6 ± 0.5	$1.20^{+0.13}_{-.11} \times 10^{11}$	700^{+2700}_{-500}
3.9.....	0.1	2.3	A, S	34.8 ± 0.7	21.3 ± 0.6	$2.69^{+0.18}_{-0.17} \times 10^{11}$	1100^{+600}_{-400}
3.10	0.3	1.8	A, S	47.2 ± 0.5	32.0 ± 0.5	$4.66^{+0.18}_{-0.17} \times 10^{11}$	1100 ± 200
3.11	0.4	1.5	A, S	65.9 ± 0.8	49.4 ± 0.7	$8.69^{+0.43}_{-0.40} \times 10^{11}$	1700 ± 200
3.12	0.6	1.5	J, S	74.2 ± 0.6	55.3 ± 0.6	$9.72^{+0.37}_{-0.35} \times 10^{11}$	2300 ± 200
3.13	0.7	1.9	J, S	61.7 ± 0.5	44.0 ± 0.5	$7.02^{+0.23}_{-0.22} \times 10^{11}$	1800^{+200}_{-100}
3.14	0.9	2.4	J, S	47.0 ± 0.5	29.9 ± 0.5	$4.00^{+0.16}_{-0.15} \times 10^{11}$	1800^{+400}_{-300}
3.15	1.0	3.1	J, S	30.0 ± 0.5	17.5 ± 0.4	$2.09^{+0.12}_{-0.11} \times 10^{11}$	1300^{+900}_{-500}
3.16	1.2	3.9	J, S	20.5 ± 0.5	10.4 ± 0.4	$1.08^{+0.10}_{-0.03} \times 10^{11}$	$>3 \times 10^{3}$
3.17	1.4	5.5	J, S	9.9 ± 0.5	4.9 ± 0.4	$(5.2 \pm 0.3) \times 10^{10}$	Thin
3.18	1.6	6.3	J, S	6.2 ± 0.5	3.3 ± 0.4	$(3.3 \pm 0.3) \times 10^{10}$	Thin
3.19	1.7	7.1	J, S	5.1 ± 0.6	2.4 ± 0.5	$(2.6 \pm 0.3) \times 10^{10}$	Thin
3.20	1.9	7.9	J, S	4.4 ± 0.6	2.4 ± 0.4	$(2.3 \pm 0.3) \times 10^{10}$	Thin
3.21	2.0	>10	J, S	3.9 ± 0.5	2.2 ± 0.5	$(2.1 \pm 0.3) \times 10^{10}$	Thin
4.0.....	−0.7	5.0	A, L, N	9.3 ± 1.5	2.4 ± 1.0	$(4.0 \pm 0.6) \times 10^{10}$	Thin
4.1.....	−0.2	3.1	A, L, N	19.9 ± 1.6	9.3 ± 1.1	$1.03^{+0.10}_{-0.06} \times 10^{11}$	Undetermined
4.2.....	0.0	2.2	A, L, N	36.0 ± 2.5	14.6 ± 1.7	$1.76^{+.25}_{-.11} \times 10^{11}$	Undetermined
4.3.....	0.3	1.5	A, L, N	55.5 ± 3.2	34.5 ± 2.2	$4.48^{+0.79}_{-0.65} \times 10^{11}$	3300^{+5400}_{-1700}
4.4.....	0.5	1.2	N	73.0 ± 4.0	52.4 ± 3.1	$8.5^{+2.1}_{-1.4} \times 10^{11}$	2600^{+1700}_{-1000}
4.5.....	0.7	1.4	J, T, N	70.7 ± 4.0	53.3 ± 3.1	$9.6^{+2.7}_{-1.7} \times 10^{11}$	2000^{+1100}_{-700}
4.6.....	0.9	2.0	J, T, N	55.9 ± 3.0	36.1 ± 2.1	$4.94^{+0.84}_{-0.68} \times 10^{11}$	2400^{+2600}_{-1100}
4.7.....	1.2	2.9	J, T, N	31.8 ± 1.9	17.2 ± 1.3	$1.89^{+0.34}_{-0.18} \times 10^{11}$	$>10^{3}$
4.8.....	1.4	3.8	J, T, N	19.2 ± 1.5	11.5 ± 1.3	$1.43^{+0.43}_{-0.32} \times 10^{11}$	$<10^{4}$
4.9.....	1.6	4.8	J, T, N	13.8 ± 1.3	8.3 ± 1.2	$1.02^{+0.60}_{-0.28} \times 10^{11}$	Undetermined
4.10	1.8	5.7	J, T, N	10.5 ± 1.1	3.5 ± 0.9	$(5.0 \pm 0.6) \times 10^{10}$	Thin
4.11	2.1	6.6	J, T, N	7.9 ± 0.9	5.4 ± 0.9	$(4.5 \pm 0.5) \times 10^{10}$	Thin
4.12	2.3	7.6	J, T, N	9.4 ± 1.1	2.2 ± 1.0	$(4.3 \pm 0.6) \times 10^{10}$	Thin
4.13	2.5	8.5	J, T, N	3.6 ± 0.9	3.6 ± 1.1	$(2.1 \pm 0.6) \times 10^{10}$	Thin
5.0.....	−3.0	5.5	A, N	13.2 ± 2.3	5.2 ± 1.5	$(6.4 \pm 1.0) \times 10^{10}$	Thin
5.1.....	−2.4	4.7	A, N	11.6 ± 2.1	5.4 ± 1.9	$(6.0 \pm 1.2) \times 10^{10}$	Thin
5.2.....	−1.7	3.8	A, N	17.4 ± 2.5	10.1 ± 1.8	$1.20^{+0.63}_{-0.34} \times 10^{11}$	Undetermined
5.3.....	−1.1	3.1	A, N	23.6 ± 2.1	10.9 ± 1.7	$1.21^{+0.19}_{-0.10} \times 10^{11}$	$>10^{3}$
5.4.....	−0.5	2.6	A, N	35.8 ± 2.4	22.4 ± 2.0	$2.91^{+0.74}_{-0.56} \times 10^{11}$	900^{+3800}_{-700}
5.5.....	0.1	2.2	A, N	40.6 ± 2.6	20.8 ± 1.9	$2.26^{+0.54}_{-0.15} \times 10^{11}$	$>3 \times 10^{3}$
5.6.....	0.7	2.1	J, N	42.5 ± 2.7	26.9 ± 2.1	$3.55^{+0.74}_{-0.61} \times 10^{11}$	1400^{+3300}_{-900}
5.7.....	1.2	2.4	J, N	43.4 ± 2.5	22.7 ± 2.0	$2.43^{+0.49}_{-0.07} \times 10^{11}$	$>3 \times 10^{3}$
5.8.....	1.8	2.9	J, N	35.4 ± 2.3	17.0 ± 1.8	$(1.89 \pm 0.40) \times 10^{11}$	$>8 \times 10^{3}$
5.9.....	2.4	3.4	J, N	25.9 ± 2.0	13.4 ± 1.6	$1.41^{+0.40}_{-0.15} \times 10^{11}$	Undetermined
5.10	3.0	4.1	J, N	22.0 ± 1.9	10.5 ± 1.7	$1.16^{+0.23}_{-0.25} \times 10^{11}$	$>10^{3}$
5.11	3.6	4.9	J, N	17.0 ± 1.6	9.8 ± 1.6	$1.15^{+0.49}_{-0.30} \times 10^{11}$	Undetermined
5.12	4.2	5.6	J, N	15.0 ± 1.7	6.0 ± 1.6	$7.6 \pm 1.0 \times 10^{10}$	Thin

TABLE 2—*Continued*

Observation Number[a]	Phase[b]	b[c] (R_{Io})	Location[d]	Wavelength of D2 (mÅ)	Wavelength of D1 (mÅ)	N (cm^{-2})	T[e] (K)
6.0.....	−0.5	5.7	A, S	3.2 ± 1.9	3.9 ± 1.7	$(2.2 \pm 1.0) \times 10^{10}$	Thin
6.1.....	−0.3	4.9	A, S	7.4 ± 2.0	5.3 ± 2.3	$(4.1 \pm 1.3) \times 10^{10}$	Thin
6.2.....	−0.2	3.9	A, S	14.8 ± 2.3	5.6 ± 1.7	$(7.2 \pm 1.1) \times 10^{10}$	Thin
6.3.....	0.0	3.1	A, S	16.5 ± 1.9	10.3 ± 1.4	$1.33^{+0.54}_{-0.38} \times 10^{11}$	$<8 \times 10^3$
6.4.....	0.1	2.3	A, S	28.4 ± 2.4	21.8 ± 2.3	$4.1^{+3.1}_{-1.3} \times 10^{11}$	100^{+100}_{-40}
6.5.....	0.3	1.9	A, S	39.3 ± 3.0	31.5 ± 3.0	$6.3^{+7.3}_{-1.9} \times 10^{11}$	200^{+300}_{-100}
6.6.....	0.4	1.6	A, S	44.9 ± 5.2	39.1 ± 5.6	$1.0^{+\inf}_{-0.6} \times 10^{12}$	$<10^3$
6.7.....	0.6	1.7	J, S	61.6 ± 4.5	42.3 ± 4.1	$6.3^{+2.1}_{-1.5} \times 10^{11}$	2100^{+3500}_{-1100}
6.8.....	0.7	2.0	J, S	55.5 ± 4.4	36.2 ± 4.1	$5.0^{+1.8}_{-1.3} \times 10^{11}$	2300^{+7500}_{-1400}
6.9.....	0.9	2.5	J, S	37.4 ± 3.9	28.6 ± 3.3	$5.2^{+6.6}_{-1.6} \times 10^{11}$	200^{+600}_{-100}
6.10	1.0	3.2	J, S	30.9 ± 4.1	17.8 ± 3.3	$2.1^{+1.2}_{-0.6} \times 10^{11}$	Undetermined
6.11	1.2	4.0	J, S	15.9 ± 3.2	7.3 ± 2.3	$(8.2 \pm 1.6) \times 10^{10}$	Thin
7.0.....	−0.2	2.3	A, N	42.3 ± 2.8	23.3 ± 2.0	$2.64^{+0.54}_{-0.37} \times 10^{11}$	$>10^3$
7.1.....	0.0	2.1	A, N	48.7 ± 3.8	28.1 ± 2.3	$3.35^{+0.73}_{-0.58} \times 10^{11}$	Undetermined
7.2.....	0.2	1.9	A, N	51.9 ± 3.2	32.1 ± 2.5	$4.14^{+0.87}_{-0.71} \times 10^{11}$	2900^{+7300}_{-1600}
7.3.....	0.4	1.9	A, N	58.6 ± 4.0	40.9 ± 2.9	$6.3^{+1.6}_{-1.2} \times 10^{11}$	1700^{+1800}_{-800}
7.4.....	0.6	1.9	J, N	65.0 ± 4.9	39.0 ± 2.8	$4.9^{+1.0}_{-0.8} \times 10^{11}$	6300^{+24500}_{-3800}
7.5.....	0.8	2.0	J, N	61.1 ± 3.5	38.1 ± 2.8	$5.0^{+1.0}_{-0.8} \times 10^{11}$	3900^{+7300}_{-2000}
7.6.....	1.0	2.2	J, N	63.2 ± 4.4	38.4 ± 2.5	$4.87^{+0.96}_{-0.77} \times 10^{11}$	$\lesssim 10^4$
7.7.....	1.3	2.5	J, N	52.9 ± 3.9	34.1 ± 2.6	$4.6^{+1.1}_{-0.8} \times 10^{11}$	2200^{+4300}_{-1300}
7.8.....	1.6	3.1	J, N	38.2 ± 2.9	25.9 ± 2.8	$3.7^{+1.5}_{-0.9} \times 10^{11}$	500^{+1700}_{-300}
7.9.....	1.9	3.6	J, N	32.5 ± 2.8	20.5 ± 2.4	$2.7^{+1.1}_{-0.6} \times 10^{11}$	600^{+5900}_{-400}
8.0.....	−0.8	7.3	L, J, N	7.7 ± 1.4	5.0 ± 1.1	$(4.4 \pm 0.7) \times 10^{10}$	Thin
8.1.....	−0.5	5.9	L, J, N	8.4 ± 1.5	4.0 ± 1.4	$(4.3 \pm 0.8) \times 10^{10}$	Thin
8.2.....	−0.1	3.6	L, J, N	22.4 ± 1.6	13.0 ± 1.4	$1.55^{+0.47}_{-0.33} \times 10^{11}$	$<5 \times 10^4$
8.3.....	0.1	2.4	L, J, N	45.8 ± 2.7	29.6 ± 2.0	$4.02^{+0.76}_{-0.63} \times 10^{11}$	1400^{+2300}_{-800}
8.4.....	0.4	1.7	L, J, N	66.0 ± 3.6	48.5 ± 2.7	$8.2^{+1.9}_{-1.3} \times 10^{11}$	1800^{+1100}_{-700}
8.5.....	0.6	1.8	T, A, N	49.5 ± 2.9	35.6 ± 2.3	$5.7^{+1.3}_{-0.9} \times 10^{11}$	900^{+800}_{-400}
8.6.....	0.9	2.7	T, A, N	28.5 ± 1.9	21.0 ± 1.5	$3.6^{+1.4}_{-0.8} \times 10^{11}$	120^{+120}_{-40}
8.7.....	1.2	4.3	T, A, N	9.0 ± 1.0	4.1 ± 0.9	$(4.6 \pm 0.5) \times 10^{10}$	Thin
8.8.....	1.4	5.5	T, A, N	3.5 ± 1.2	2.8 ± 1.2	$(2.1 \pm 0.7) \times 10^{10}$	Thin
8.9.....	1.6	7.0	T, A, N	4.4 ± 1.0	1.8 ± 0.8	$(2.2 \pm 0.5) \times 10^{10}$	Thin
9.0.....	−1.7	>10	L, N	0.9 ± 0.4	1.6 ± 0.6	$(5.9 \pm 3.4) \times 10^{9}$	Thin
9.1.....	−1.5	>10	L, N	0.6 ± 0.5	2.7 ± 0.5	$(7.8 \pm 3.1) \times 10^{9}$	Thin
9.2.....	−1.3	9.1	L, N	0.9 ± 0.4	1.1 ± 0.6	$(5.5 \pm 3.4) \times 10^{9}$	Thin
9.3.....	−1.1	8.4	L, N	1.3 ± 0.6	0.8 ± 0.6	$(6.8 \pm 3.6) \times 10^{9}$	Thin
9.4.....	−0.9	7.5	L, N	2.1 ± 0.8	1.0 ± 0.7	$(1.1 \pm 0.4) \times 10^{10}$	Thin
9.5.....	−0.7	6.4	L, N	4.7 ± 1.2	3.9 ± 0.9	$(2.9 \pm 0.5) \times 10^{10}$	Thin
9.6.....	−0.4	5.3	L, N	7.4 ± 0.9	2.8 ± 0.5	$(3.5 \pm 0.4) \times 10^{10}$	Thin
9.7.....	−0.2	4.2	L, N	13.6 ± 1.2	6.4 ± 0.9	$(7.1 \pm 0.6) \times 10^{10}$	Thin
9.8.....	0.0	3.1	L, N	22.6 ± 1.5	14.3 ± 1.2	$1.91^{+0.47}_{-0.37} \times 10^{11}$	200^{+800}_{-100}
9.9.....	0.2	2.3	L, N	36.7 ± 2.2	28.6 ± 1.7	$5.5^{+2.6}_{-1.2} \times 10^{11}$	200^{+200}_{-100}
9.10	0.4	2.0	L, N	46.0 ± 2.6	31.7 ± 1.8	$4.69^{+0.87}_{0.68} \times 10^{11}$	900^{+1000}_{-400}
9.11	0.7	2.1	T, N	35.6 ± 2.2	22.3 ± 1.5	$2.88^{+0.55}_{-0.43} \times 10^{11}$	900^{+2400}_{-600}
9.12	0.9	2.8	T, N	21.5 ± 1.7	12.2 ± 1.0	$1.41^{+0.33}_{-0.24} \times 10^{11}$	$<6 \times 10^4$
9.13	1.1	3.8	T, N	7.9 ± 1.0	7.2 ± 1.0	$(4.9 \pm 0.6) \times 10^{10}$	Thin
9.14	1.3	4.8	T, N	4.8 ± 0.9	3.6 ± 0.9	$(2.7 \pm 0.5) \times 10^{10}$	Thin
9.15	1.5	5.9	T, N	2.6 ± 0.9	2.6 ± 0.8	$(1.7 \pm 0.5) \times 10^{10}$	Thin
9.16	1.7	7.1	T, N	0.7 ± 0.7	0.9 ± 0.5	$(5.6 \pm 3.3) \times 10^{9}$	Thin
9.17	1.9	8.2	T, N	0.8 ± 0.7	1.3 ± 0.7	$(6.2 \pm 4.2) \times 10^{9}$	Thin
9.18	2.2	8.9	T, N	0.7 ± 0.8	-2.0 ± 0.9	$3.7^{+4.3}_{-3.7} \times 10^{9} x$	Thin
9.19	2.4	9.4	T, N	0.5 ± 1.0	0.9 ± 1.0	$3.6^{+6.0}_{-5.0} \times 10^{9}$	Thin
10.1	−0.9	6.1	A, L, S	8.3 ± 1.0	<5	$(4.4 \pm 0.6) \times 10^{10}$	Thin
10.2	−0.3	3.7	A, L, S	17.8 ± 1.5	11.1 ± 1.5	$1.44^{+0.56}_{-0.40} \times 10^{11}$	$<10^4$
10.3	0.2	1.6	A, L, S	39.4 ± 4.0	24.3 ± 10.0	$3^{+8}_{-1} \times 10^{11}$	Undetermined
10.4	0.7	1.5	J, T, S	21.8 ± 4.0	15.7 ± 2.0	$2.5^{+2.4}_{-0.9} \times 10^{11}$	$<10^3$

NOTE.—Table 2 is also available in machine-readable form in the electronic edition of the *Astrophysical Journal*.

[a] Observation number is in the form $X.Y$, where X is the eclipse number as given in Table 1 and Y is the number of the spectrum taken in the event series.

[b] The eclipse phase of an observation is defined as the fraction of the event completed at the midpoint of the observation. Negative eclipse phase refers to observations made before penumbral contact; phases greater than 1 refer to observations after final contact.

[c] The uncertainties in the impact parameter are $\lesssim 0.1 R_{Io}$.

[d] Location sampled relative to Io. L = leading hemisphere; T = trailing hemisphere; J = sub-Jupiter hemisphere; A = anti-Jupiter hemisphere; N = north of Io; and S = south of Io.

[e] Approximate coronal temperature. Thin: optically thin, with no temperature estimate possible. Undetermined: optically thick, but no temperature estimate possible due to poor data quality.

ent objects, the removal was accomplished by vertically shifting the hot-star continuum until an agreement was obtained with line depths of object spectra.

Finally, having produced "dry" spectra of satellites in and out of eclipse, the former were divided by the latter in order to reveal isolated eclipse features produced by Io. Some pronounced residual noise exists at the location of the precise core of the solar sodium lines, but fortunately one can stay clear of these pathological regions since they affect only the very shallow wings of the isolated eclipse features. The signal-to-noise ratio was determined from continuum regions on both sides of and some 10–30 pixels away from the Fraunhofer core location in each spectrum. Stated as an rms value [rms = 1/(S/N)], this quantity was used in the computation of 1 σ error bars for the equivalent width as follows: $\Delta W = (n_{\rm pix})^{1/2}{\rm rms}\, d\lambda$, where $n_{\rm pix}$ is the base width of the line in pixels and $d\lambda$ is the size of a pixel in the same wavelength unit as that of ΔW.

Thorium lamps have been employed to determine the wavelength calibration. The dispersion is found by a polynomial fit to the positions of identified (i.e., with known laboratory wavelengths) thorium lines.

2.3. *Catalina Observatory Observations*

A single event was observed from the Catalina Observatory outside of Tucson, Arizona, using the Lunar and Planetary Laboratory Echelle Spectrometer. The eclipses in 1991 occurred close to Jupiter's solar conjunction, making observations extremely difficult. Therefore, although the spectral resolution of the data is quite high ($\lambda/\Delta\lambda \sim 100{,}000$), these data are of a poorer quality than the other events. Additionally, the 139 s exposures have lower signal-to-noise ratios. This event, however, does provide another time period that can be used to search for long-term variability in the corona. These data were reduced using methods similar to those described above.

3. ANALYSIS

Each exposure scanned a different narrow region of Io's atmosphere. To first order, the region can be characterized by the "closest approach distance" between Io and the line connecting the Sun to the eclipsed satellite (commonly called the impact parameter; see Fig. 1). In reality, the sampled region is broadened by the angular size of the Sun, the finite size and visible appearance of the eclipsed satellite, and the motion of the satellite during an exposure. The distribution of impact parameters during an exposure was calculated analytically by the method of Mallama (1991) using the G-5 ephemerides (Arlot et al. 1982; Arlot 1996) as well as the satellite limb-darkening model and albedo patterns from Mallama (1991). The distributions are computed for the continuum wavelength bracketing the absorption feature and are independent of the data. Sodium in the corona does not affect these distributions since the absorption feature is narrow and does not significantly change the shape or brightness of the continuum.

Each exposure's distribution yielded a mean impact parameter and a standard deviation indicative of the width of the distribution during an exposure. The absorption equivalent width of each observation is assigned to the mean impact parameter. The broadening effects listed above can be broken into two categories and quantified. First, instantaneous spreading of light is due to the effects of the finite size of the eclipsed object and the angular size of the Sun. Figure 4*a* shows the instantaneous distributions for three times during an eclipse. The amount of spreading is determined by the standard deviation of an instantaneous distribution. The width of the region (2 times the standard deviation) is generally between $0.8R_{\rm Io}$ and $1.6R_{\rm Io}$ and can vary somewhat during an event. A second effect, smearing during an integration, depends on the relative tangential velocities of the satellites and the exposure times and amounts to $\sim$800 km, or $0.4R_{\rm Io}$. Note that these effects do not correspond to the uncertainty in the impact parameter since the distributions themselves are well determined. Figure 4*b* shows the effect of satellite motions during an exposure on the distribution. The similarity between the average distribution (*dashed line*) and the instantaneous distribution at the event midpoint (*solid line labeled "midpoint"*) shows that the smearing due to satellite motion is small compared to the spreading of the light as observed at the Earth.

The timing of each event was determined by Arlot (1996). The uncertainty in the prediction of the event midpoint is 5–15 s, corresponding to $\sim$150 km in the positions of the satellites (J.-E. Arlot 2000, personal communication). This implies an uncertainty in the prediction of the impact parameter of $\lesssim 0.1\ R_{\rm Io}$. The 63 s difference between Universal Time (UT) and Terrestrial Dynamical Time has been taken into account for comparison of the times of observations and the ephemeris time. Although the strength of the sodium absorption is likely to vary across the eclipsed

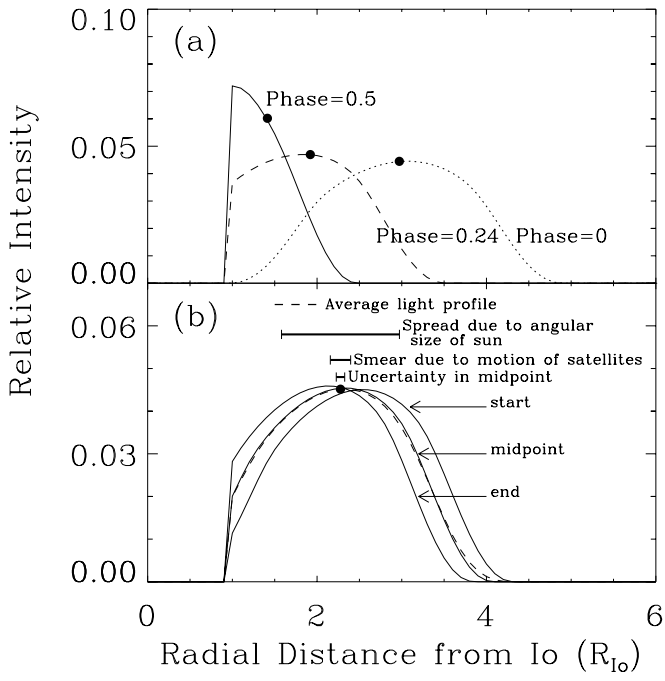

FIG. 4.—Distribution of the light passing Io. (*a*) Instantaneous distribution of impact parameters near Io at three times (phases) during an eclipse. The point marked on each distribution represents the average distance from Io of the light distribution (the impact parameter) as described in the text. (*b*) Change in the impact parameter distribution during an observation. Distributions are shown for the beginning, middle, and end of a typical observation. Dashed profile is the average for the observation. The impact parameter for this profile is marked. Scale bars are given for the uncertainty in the determination of the impact parameter ($2\ \sigma_b \sim 0.1R_{\rm Io}$), the amount of smearing due to motion of the satellites during the observation ($\sim 0.2R_{\rm Io}$ for this observation), and the spread of light due to the Sun's angular size ($\sim 1.4R_{\rm Io}$).

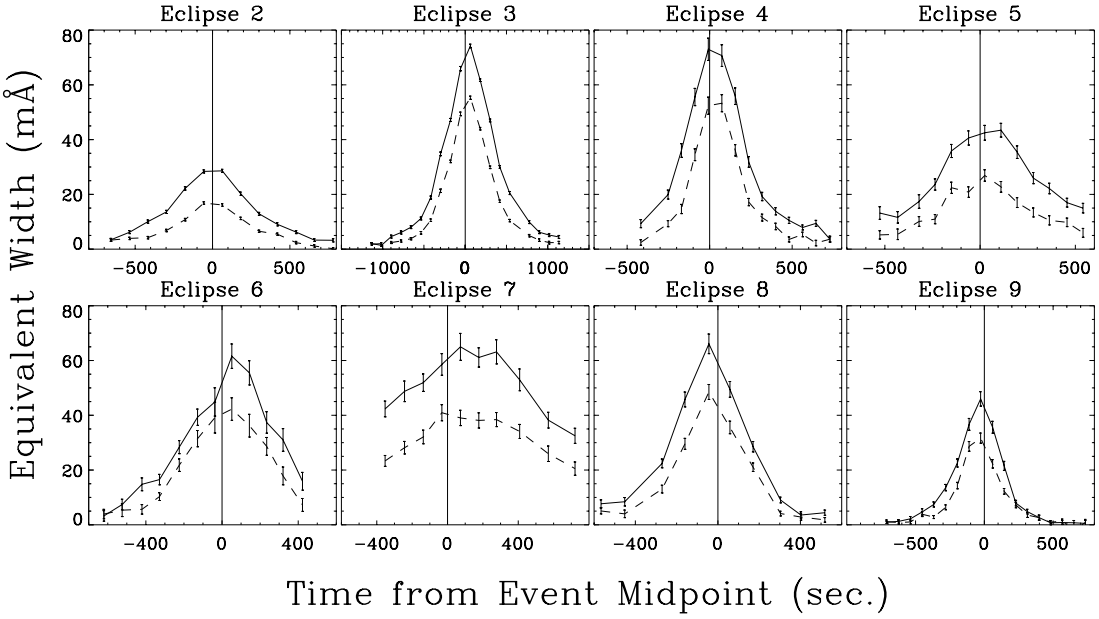

FIG. 5.—Equivalent width vs. the time from the event midpoint for the 1997 mutual events. For each event, solid lines show the D_2 equivalent widths and dashed line shows the D_1 equivalent widths. Note that events are not symmetric about time = 0, indicative of column density asymmetries in the corona.

satellite and during the exposure, departures from linearity are small compared to the error in individual measurements and are therefore neglected.

The column of absorbing sodium was derived by a comparison of the equivalent widths of the sodium D_2 and D_1 resonance lines ($3s\ ^2S_{1/2} \rightarrow 3p\ ^2P_{1/2},3p\ ^2P_{3/2}$) at 5889.92 and 5895.95 Å, respectively. The continuum was determined by fitting a line to the region surrounding the absorption line, and the sum was performed only in the pixel region containing the line. The equivalent widths calculated for each spectrum are listed in Table 2 and plotted in Figure 5 versus time.

The equivalent width expected for a given value of the column density and the temperature was computed as discussed in Brown & Yung (1976). For low column densities (with optical depth $\tau \lesssim 1$ or column density $N \lesssim 10^{11}$ cm^{-2}), the equivalent width is independent of temperature and depends only on the column density. In this case, the column density listed in Table 2 is the average of the abundances computed independently for the D_2 and D_1 lines weighted by the uncertainties in the measurements.

The degeneracy in temperature is lifted as the absorbing column increases. Therefore, to determine the column density in the optically thick case, it was necessary to consider the two absorption lines together. For a given pair of D_2 and D_1 equivalent widths, there is a unique column density and temperature that produces the absorptions. We computed these values by plotting curves of the column density required to produce the measured equivalent width versus temperature for each of the measured lines (Fig. 6). The intersection of the two curves is the unique column density and temperature. The error ellipse in the D_1 versus D_2 plot was mapped onto the N versus T plot. The extrema of this ellipse gave the 1 σ errors in temperature and column density, listed in Table 2.

4. DISCUSSION

The column densities derived from our comparison of the sodium D_1 and D_2 equivalent widths are plotted in Figure 7 versus the impact parameter of the observations and are listed in Table 2. Also listed are temperature estimates for observations of optically thick regions of the corona. Plotted over the data in Figure 7 are the best-fit power-law functions to all the 1997 data that have an impact parameter less than $5.6R_{Io}$ (except as noted below) and the best-fit power law from to the data of Schneider et al. (1991). The outer boundary was chosen to conform with the limits used by Schneider et al. (1991), who looked at differences between the profile inside and outside of Io's Hill sphere, the effective limit of Io's gravity located at $5.6R_{Io}$. The best spherically symmetric fit to the data is given by

$$N(b) = (2.2^{+1.4}_{-0.7} \times 10^{12}) b^{-2.34^{+0.27}_{-0.34}}\ \text{cm}^{-2}\ . \quad (1)$$

Fitting a power law to the data of Schneider et al. (1991) gives a column density profile of

$$N(b) = (2.4^{+1.1}_{-0.6} \times 10^{12}) b^{-2.48^{+0.27}_{-0.32}}\ \text{cm}^{-2}\ , \quad (2)$$

which fits the current data within the uncertainty. This indicates that there have been no significant changes in the directionally averaged corona in the 12 yr between measurements. However, as discussed below, there are event-to-event fluctuations in the column density profile. Note that outside $\sim 6R_{Io}$, the corona column density becomes more variable. This is due to a combination of higher noise in the data (due to weaker absorption lines) and real variability in the corona outside of Io's Hill sphere.

An indication that the corona did not vary significantly during the period between the 1985 and 1997 measurements is a mutual event observation from 1991. Only four spectra from the 1991 Catalina Observatory event (event 10) show any measurable absorption. The column densities determined from this event are shown in Figure 7, although they are not included in the fit shown by the solid line. Despite the relatively poor signal-to-noise ratio of the data, which makes precise column density values difficult to determine, the column densities measured are consistent with those seen in both the 1985 (Schneider et al. 1991) and 1997 data. This is a further indication of temporal stability in the

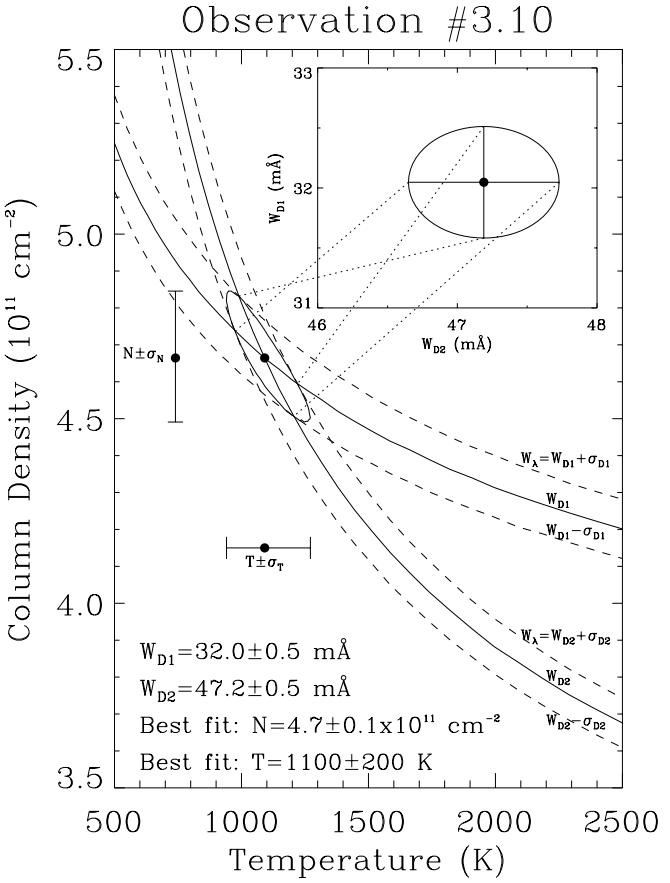

FIG. 6.—Curves of constant equivalent width as a function of temperature and column density. Solid lines show column density vs. temperature for the measured D_2 and D_1 equivalent widths; dashed lines are for the 1 σ errors on the equivalent widths. The intersection of the two solid lines gives the unique column density and temperature required to produce absorption lines with the measured equivalent widths. The error ellipse in column density and temperature is shown. The 1 σ error bars on N and T are given by the extrema of the ellipse. The insert shows the D_2 and D_1 equivalent widths and their errors for the observation. Dotted lines show how the errors in equivalent width map onto the N vs. T space.

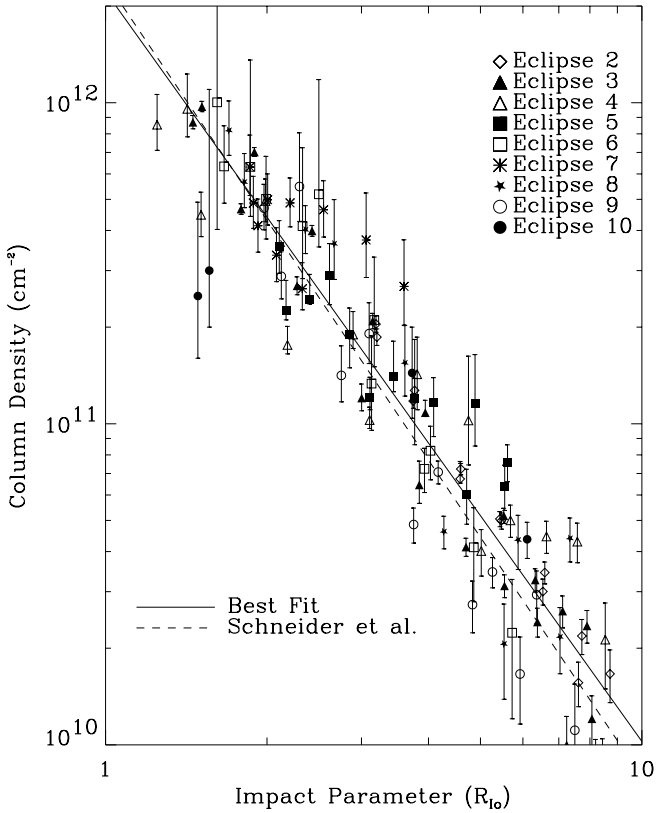

FIG. 7.—Column density vs. impact parameter for all data with measurable equivalent widths. The best-fit power law to the 1997 data within 5.6R_{Io} (eq. [1]) is plotted with a solid line. Dashed line shows the result of Schneider et al. (1991; eq. [2]). Four column density measurements from 1991 May 21 are shown but are not included in power-law fit. Event 1, listed in Table 1, is not shown (see text for explanation).

corona, although we were not able use this data to look for spatial asymmetries in the corona. Unfortunately, the observations that measured closest to Io were made when Europa was in Io's umbra, reducing Europa's brightness and, consequently, the signal-to-noise ratio of the data.

Io was very close to superior heliocentric conjunction for the event of 1997 June 21 (event 1), making it difficult to interpret. Because the radial velocity difference between Io and the Sun was very small, the resolution of the instrument was not great enough to separate the Iogenic absorption from the solar Fraunhofer line with certainty for most of the observations. However, for some of the observations within $\sim 2.5R_{Io}$, where the absorption from the corona is stronger, the equivalent widths were more easily measured. These data are listed in Table 2. The column densities derived agree qualitatively with the general column density profile in the corona, although the systematic errors introduced in the reduction make quantitative analysis impossible.

The temperature of the corona is estimated to be 1600 K with a 1 σ confidence level between 1200 and 3600 K. The uncertainties in the data are too large to determine a radial temperature profile. Schneider et al. (1991) measured a temperature of $\sim$2000 K. This is consistent with the current measurement, given the wide temperature range estimated from the individual observations as shown in Table 2. Our measurement is also consistent with previous model predictions for the temperature. Summers et al. (1989) determined that previous observations were consistent with a corona with a temperature of $\sim$1000 K but do not give an upper limit on the temperatures that would be consistent with the data. A model that includes solar heating, plasma heating, and Joule heating of the atmosphere predicts temperatures of $\sim$1800 K in the corona (Strobel, Zhu, & Summers 1994). Depending on Io's orbital phase and the solar zenith angle, Wong & Smyth (2000) predict exobase temperatures of between 220 and 2800 K for an SO_2 sublimation atmosphere.

Although we do not see any evidence for long-term temporal variability in the corona, we have detected a possible asymmetry in the radial column density profile. Most of the events compare to varying degrees the contrast between Io's inner (sub-Jupiter) and outer (anti-Jupiter) hemispheres (Fig. 8*a*). For seven of the eight events considered, the sub-Jupiter hemisphere is denser than the anti-Jupiter hemisphere. The two hemispheres had identical column density profiles during event 2. Figure 9 shows the D_2 equivalent widths versus impact parameters for eight mutual events. For each event, the solid lines show absorption from the sub-Jupiter hemisphere and the dashed lines show the anti-Jupiter hemisphere. With the exception of event 2, the spectra from the inner hemisphere show more absorption

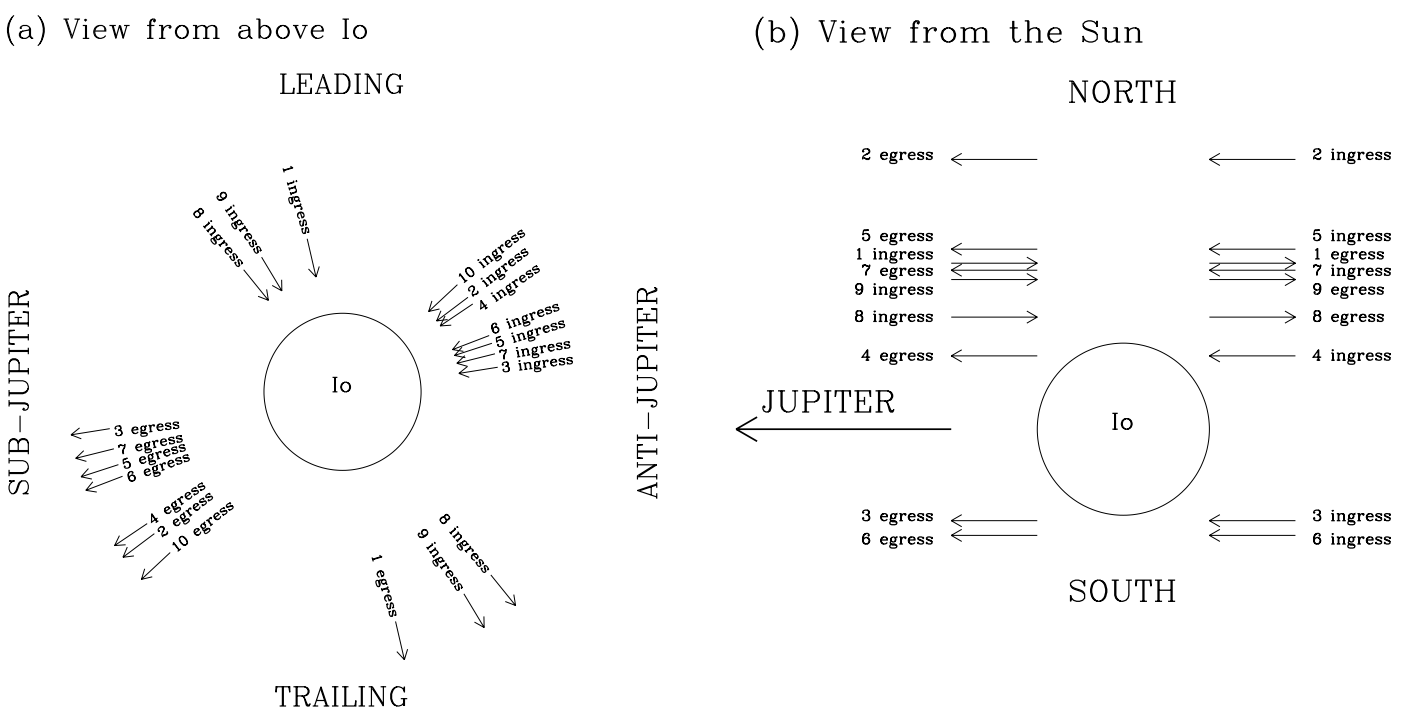

FIG. 8.—Eclipse geometry for each event. (*a*) Paths of each eclipse in fixed Io coordinates as seen from above Io's north pole. The inbound (ingress) and outbound (egress) portions of each eclipse are shown. Observation lines of sight are perpendicular to the eclipse path in the plane of the page. (*b*) Paths of each event as seen from the Sun. The lines of sight are perpendicular to the eclipse paths into the page.

than the outer hemisphere for measurements at similar radial distances from Io. The D_1 equivalent widths follow a similar trend. Figure 10 shows the column density asymmetry between the inner and outer hemispheres of Io. The dashed line shows the "average" corona column density on the anti-Jupiter hemisphere; the solid line is a fit to the sub-Jupiter hemisphere. The best fits to the inner and outer coronae are given by

sub-Jupiter (inner) hemisphere:

$$(3.0^{+0.9}_{-0.4} \times 10^{12}) b^{-2.42^{+0.15}_{-0.26}} \text{ cm}^{-2} , \quad (3)$$

anti-Jupiter (outer) hemisphere:

$$(1.8^{+0.8}_{-0.6} \times 10^{12}) b^{-2.29^{+0.42}_{-0.27}} \text{ cm}^{-2} . \quad (4)$$

The anti-Jupiter corona is on average 60% as dense as the corona on the sub-Jupiter side at the same radial distance from Io. The steepnesses of the column density profiles are similar for the opposite sides of Io. Schneider et al. (1991) did not detect this asymmetry, although the uncertainties in their data were greater. The uncertainties given in equations (3) and (4) are representative of event-to-event variations in the data.

Event 7 from McDonald Observatory is unique in that it is the only event that occurred close to Io's eastern elongation. This event shows a similar asymmetry to the other events discussed; namely, the sub-Jupiter hemisphere is more dense than the anti-Jupiter hemisphere. Therefore, we conclude that we detect an inner/outer asymmetry rather than an east/west asymmetry. Event 7 is anomalously dense on the sub-Jupiter hemisphere compared to the other events. Since this is the only event observed in this geometry, we cannot determine whether this is a true east/west column density variation or simply representative of short-term temporal variability in the corona. This column density anomaly could also be due to an uncorrected systematic error in the data. This would explain also the difficulties in constraining temperature (see Table 2). However, we still conclude that this event displays an inner/outer asymmetry since the asymmetry is clearly seen in the equivalent widths (Fig. 9). The asymmetry appears in both the sodium D_2 and D_1 equivalent widths. Therefore, despite any possible difficulties in determining the precise column densities for this event, the spectra reveal asymmetric absorption. Although ideally we would like more observations at eastern elongation, the available data better support an inner/outer asymmetry than an east/west asymmetry.

Event 9 is listed in Table 2 as measuring leading/trailing differences. Although this event occurs close to Io's inferior conjunction (Fig. 3) and therefore is most suited to measuring differences between the leading and trailing hemispheres (see Fig. 8*a*), it does measure some differences between the inner and outer hemispheres and so has been included in this analysis. Similarly, the other events, which primarily compare the inner and outer hemispheres, are also sensitive to leading and trailing asymmetries. The conclusion that we have detected an inner/outer asymmetry rather than a leading/trailing asymmetry is supported by the fact that different events measure different combinations of the regions near Io. For example, event 4 measures the outer/leading hemisphere in the first half of the event and the inner/trailing hemisphere in the second. Event 8 probes the inner/leading hemisphere first and the outer/trailing last. The inner hemisphere is more dense for each of these events, regardless of whether the leading or trailing hemisphere is also being observed.

We are not able to rule out the possibility of a leading/trailing asymmetry in addition to the inner/outer asymmetry, but there is no clear evidence that this is the case.

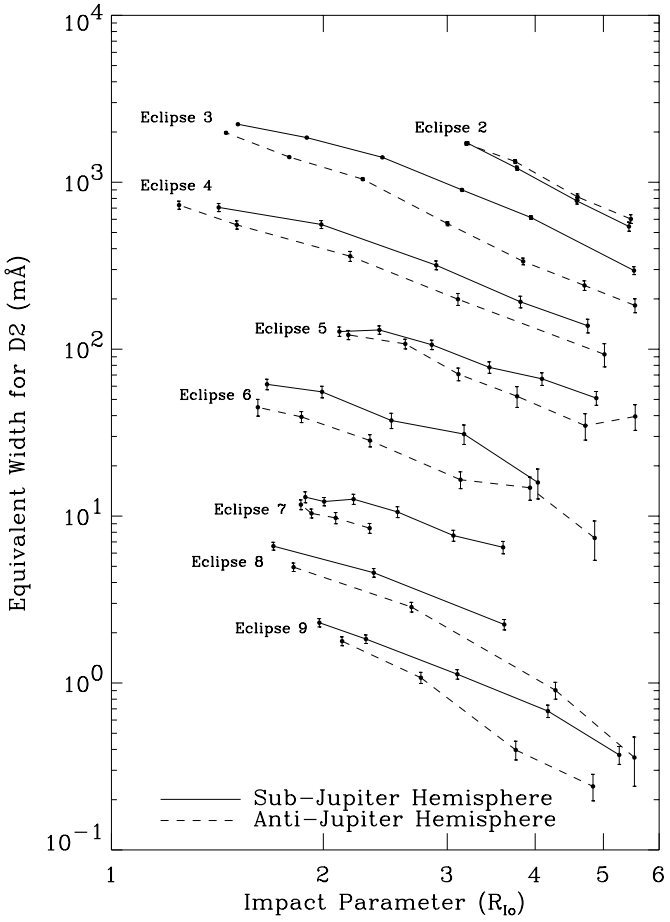

FIG. 9.—Sodium D2 equivalent width vs. impact parameter for seven of the mutual events observed. For each event, solid lines indicate measurements from Io's sub-Jupiter hemisphere and dashed lines show the anti-Jupiter hemisphere. The events have been vertically separated for clarity. Eclipses 2, 3, 4, 5, 7, 8, and 9 have been offset by factors of 60, 30, 10, 3, 1/5, 1/10, and 1/20, respectively. Eclipse 6 has not been shifted.

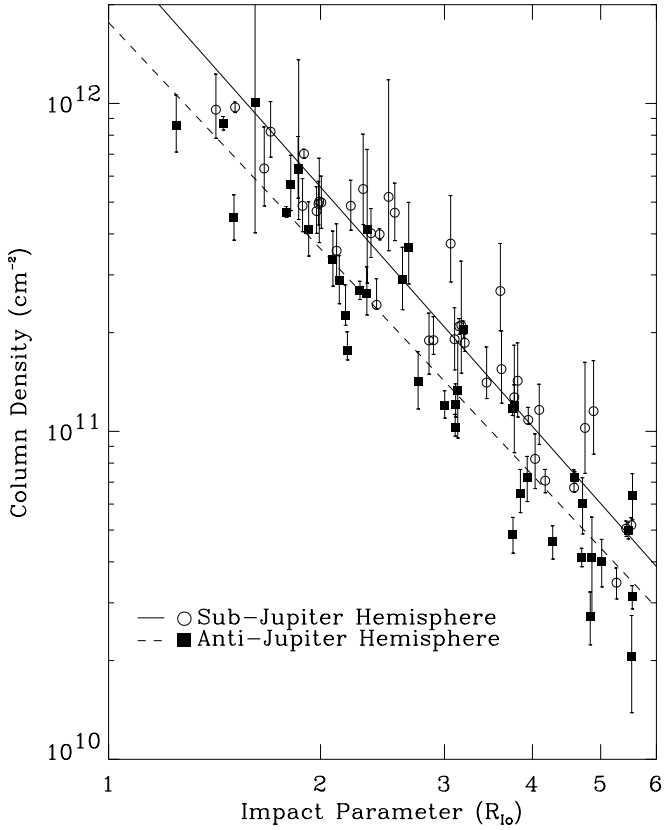

FIG. 10.—Column density vs. impact parameter showing the inner/outer column density asymmetry. *Circles*: Measurements from Io's sub-Jupiter hemisphere; *squares*: the anti-Jupiter hemisphere. The solid line show a power-law fit to the circles; i.e., the solid line is the average coronal column density over the sub-Jupiter hemisphere. Dashed line represents the average anti-Jupiter corona. The sub-Jupiter hemisphere is 1.7 times as dense as the anti-Jupiter hemisphere.

The two events that best measure leading/trailing differences, events 8 and 9, both show higher column density over the leading hemisphere than the trailing. However, events 3, 4, 5, 6, and 7, which measure leading/trailing differences to lesser degrees, show higher trailing densities. Therefore, it appears that there are no persistent column density differences between the leading and trailing hemispheres. The events that best measure the differences between the inner and outer hemispheres, events 3, 5, 6, and 7, all measure higher column densities above the sub-Jupiter hemisphere than above the anti-Jupiter hemisphere. Unfortunately, the events that best measure differences between the leading and trailing hemispheres occur when the radial heliocentric velocity is lowest and the absorption is most difficult to separate from the solar Fraunhofer line.

Asymmetries in the corona point to asymmetries in the processes that affect slow sodium. These could be related to the creation or loss of neutral sodium in the corona. A density asymmetry would arise if the source rate on the sub-Jupiter side or the loss rate on the anti-Jupiter side is enhanced. Another possibility is that the velocity of escaping neutrals is greater for the anti-Jupiter hemisphere. This would also result in a greater column density of sodium in the sub-Jupiter corona and most likely result in a shallower profile for the anti-Jupiter hemisphere. This change in slope is not seen, although the uncertainties in the determination of the slope may be large enough that a difference in slope between the two hemispheres cannot be seen.

A smaller source rate on the anti-Jupiter hemisphere is suggested by observations of Io's auroral emissions ("equatorial spots"): the anti-Jupiter spot is ~20% brighter than the sub-Jupiter spot (Roesler et al. 1999; Retherford et al. 2000). Saur et al. (2000) have modeled the electron flow past Io to show that the Hall effect close to Io results in more energy deposited to the anti-Jupiter side than the sub-Jupiter side. In the context of the auroral oxygen emissions, there is more electron impact excitation on the anti-Jupiter side, resulting in a brighter equatorial spot. This same effect would result in a greater sodium ionization rate since the ionization potential of sodium is lower than that of oxygen. Since the equatorial spots are observed near Io's surface (within $\sim 1R_{Io}$–$2R_{Io}$), only sodium in that region would most likely be affected. Therefore, the amount of escaping neutral sodium would be preferentially reduced on the anti-Jupiter hemisphere, and the column density further out in the corona would be smaller. The slope of the corona, however, would not be affected.

The fast sodium jet observed by Wilson & Schneider (1999) and Burger et al. (1999) is most likely not directly responsible for this asymmetry. Fast sodium would show up as a broad Doppler-shifted feature well below the detection limit. However, it is possible that the escape of fast sodium

affects the sputtering rates from Io or the velocity of escaping slow neutrals.

If the corona does, in fact, have an inner/outer asymmetry, then there is a question as to why event 2 appears to be radially symmetric about Io. Understanding this event requires additional observations at large distances from the poles and modeling beyond the scope of this paper. A possible explanation may lie in the fact that this event measures the corona farther above Io's north pole than any of the other events (Fig. 8*b*), which might suggest that the processes that cause the asymmetry are acting closer to Io's equatorial region than the polar regions. However, there are other events that measure the corona north of Io, and these events do not support this hypothesis in that we would expect a relationship between the degree of asymmetry and the minimum impact parameter of the event.

There are event-to-event fluctuations in the coronal column density profile. Although the deviations in measured column density are small compared with the mean column density, they are greater than the uncertainties in the individual measurements. Additionally, as discussed, the inner/outer asymmetry is persistent, indicating that when the corona is in a denser state, the column density is increased on both the Jupiter and anti-Jupiter sides. The measured standard deviation in the corona column density at a distance of $3R_{\rm Io}$ is $\sim$25% of the mean column density at this distance. Above Io's sub-Jupiter hemisphere, the mean column density at $3R_{\rm Io}$ is 2.3×10^{11} cm^{-2} with a standard deviation of 0.6×10^{11} cm^{-2}. The variation is proportionately the same above the anti-Jupiter hemisphere: at $3R_{\rm Io}$ the mean column density is $(1.5 \pm 0.4) \times 10^{11}$ cm^{-2}.

5. SUMMARY

This study shows that there have been no significant global changes in Io's sodium corona since the previous study of the column density profile (Schneider et al. 1991). Measurements of the coronal column density from 1985, 1991, and 1997 all show the same roughly spherically symmetric sodium corona within six Io radii of Io.

The average corona is well described as a spherically symmetric cloud around Io with a column density profile of

$$N(b) = (2.2^{+1.4}_{-0.7} \times 10^{12}) b^{-2.34^{+0.27}_{-0.34}} \text{ cm}^{-2} , \quad (5)$$

where b is the impact parameter of the observation in Io radii. This corresponds to a radial density profile of

$$n(r) = 6700 r^{-3.34} \text{ cm}^{-3} , \quad (6)$$

with r the distance from Io in Io radii.

There is evidence, however, for a persistent asymmetry in the corona. The events that measure nearest Io's equator indicate that the corona above Io's sub-Jupiter hemisphere is $\sim$1.7 times as dense as the corona above the hemisphere that faces away from Jupiter. This result may be consistent with the observations of Io's auroral emissions as explained by Saur et al. (2000). Additionally, smaller event-to-event fluctuations of $\sim$25% are seen in the coronal column density.

Theoretical studies of the corona and neutral clouds have always used symmetric loss from Io. Smyth & Combi (1997) modeled the spherically symmetric sodium corona described by Schneider et al. (1991) with symmetric loss, although they did determine that the corona has an asymmetric density profile when the sodium directional feature is aligned along Io's orbital plane. However, our observing method is not sensitive to an asymmetry caused by the directional feature. Cremonese et al. (1998) found spherically symmetric loss from Io most consistent with the observational data, including the observations of Schneider et al. (1991) and high-resolution spectra of sodium near Io. The data presented here are the highest quality observations made of the sodium column abundance in Io's corona and indicate that the loss from Io may in fact not be as symmetric as previously thought. Future work is needed to determine the reason for the observed asymmetry.

REFERENCES

Arlot, J.-E. 1996, A&A, 314, 312
Arlot, J.-E. 1982, A&A, 107, 305
Ballester, G. E., et al. 1987, ApJ, 319, L33
Brown, R. A. 1974, in Exploration of the Planetary System, ed. A. Woszczyk & C. Iwaniszewska (Boston: Reidel), 527
———. 1981, ApJ, 244, 1072
Brown, R. A., Goody, R. M., Murcray, F. J., & Chaffee, F. C. 1975, ApJ, 200, L49
Brown, R. A., & Yung, Y. L. 1976, in Jupiter, ed. T. Gehrels (Tucson: Univ. Arizona Press), 1102
Burger, M. H., Schneider, N. M., & Wilson, J. K. 1999, Geophys. Res. Lett., 26, 3333
Cremonese, G., Marzari, F., Eccli, N., & Corrain, G. 1998, Icarus, 131, 138
Feldman, P. D., et al. 2000, Geophys. Res. Lett., 27, 1787
Hinson, D. P., et al. 1998, J. Geophys. Res., 103, 29343
Lellouch, E. 1996, Icarus, 124, 1
Mallama, A. 1991, Icarus, 92, 324
McGrath, M. A., Belton, M. J. S., Spencer, J. R., & Sartoretti, P. 2000, Icarus, 146, 476
Moore, C. E., Minnaert, M. G. J., & Houtgast, J. 1966, in NBS Monograph 61, The Solar Spectrum 2935 Å to 8770 Å, 259
Retherford, K. D., Moos, H. W., Strobel, D. F., Wolven, B. C., & Roesler, F. L. 2000, J. Geophys. Res., 105, 27157
Roesler, F. L., et al. 1999, Science, 283, 353
Saur, J., Neubauer, F. M., Strobel, D. F., & Summers, M. E. 2000, Geophys. Res. Lett., 27, 2893
Schneider, N. M., Hunten, D. M., Wells, W. K., Schultz, A. B., & Fink, U. 1991, ApJ, 368, 298
Schneider, N. M., Hunten, D. M., Wells, W. K., & Trafton, L. M. 1987, Science, 238, 55
Smyth, W. H. 1992, Adv. Space. Res., 12, 337
Smyth, W. H., & Combi, M. R. 1997, Icarus, 126, 58
Spencer, J. R., & Schneider, N. M. 1996, Annu. Rev. Earth Planet. Sci., 24, 125
Strobel, D. F., Zhu, X., & Summers, M. E. 1994, Icarus, 111, 18
Summers, M. E., Strobel, D. F., Yung, Y. L., Trauger, J. T., & Mills, F. 1989, ApJ, 343, 468
Thomas, N. 1996, A&A, 313, 306
Trafton, L. T., Parkinson, T., & Macy, W., Jr. 1974, ApJ, 190, L85
Vogt, S. S. 1994, in UCO/Lick Observatory Tech. Rep. 67, HIRES User's Manual
Wilson, J. K., & Schneider, N. M. 1994, Icarus, 111, 31
———. 1999, J. Geophys. Res., 104, 16567
Wolven, B. C., et al. 2001, J. Geophys. Res., in press
Wong, M. C., & Smyth, W. H. 2000, Icarus, 146, 60